CHEMISTRY OF MATERIALS

pubs.acs.org/cm

Article

Solvent and A-Site Cation Control Preferred Crystallographic Orientation in Bromine-Based Perovskite Thin Films

Juanita Hidalgo, Yu An, Dariia Yehorova, Ruipeng Li, Joachim Breternitz, Carlo A.R. Perini, Armin Hoell, Pablo P. Boix, Susan Schorr, Joshua S. Kretchmer,* and Juan-Pablo Correa-Baena*

Cite This: *Chem. Mater.* 2023, 35, 4181−4191

Read Online

ACCESS | Metrics & More | Article Recommendations | Supporting Information

ABSTRACT: Preferred crystallographic orientation in polycrystalline films is desirable for efficient charge carrier transport in metal halide perovskites and semiconductors. However, the mechanisms that determine the preferred orientation of halide perovskites are still not well understood. In this work, we investigate crystallographic orientation in lead bromide perovskites. We show that the solvent of the precursor solution and organic A-site cation strongly affect the preferred orientation of the deposited perovskite thin films. Specifically, we show that the solvent, dimethylsulfoxide, influences the early stages of crystallization and induces preferred orientation in the deposited films by preventing colloidal particle interactions. Additionally, the methylammonium A-site cation induces a higher degree of preferred orientation than the formamidinium counterpart. We use density functional theory to show that the lower surface energy of the (100) plane facets in methylammonium-based perovskites, compared to the (110) planes, is the reason for the higher degree of preferred orientation. In contrast, the surface energy of the (100) and (110) facets is similar for formamidinium-based perovskites, leading to lower degree of preferred orientation. Furthermore, we show that different A-site cations do not significantly affect ion diffusion in bromine-based perovskite solar cells but impact ion density and accumulation, leading to increased hysteresis. Our work highlights the interplay between the solvent and organic A-site cation which determine crystallographic orientation and plays a critical role in the electronic properties and ionic migration of solar cells.

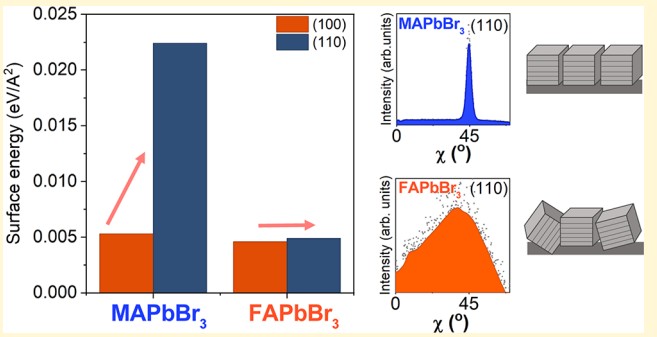

INTRODUCTION

Preferred crystallographic orientation in polycrystalline films is highly desired for efficient charge carrier transport in organic−inorganic lead halide perovskite solar cells. Oriented crystallographic domains have been shown to enhance charge carrier transport[1] and suppress ionic migration[2] in lead halide perovskite films. Therefore, manipulating the degree of crystallographic orientation presents an important design principle.[3−5] Furthermore, organic−inorganic lead bromide perovskites, compared to the more common lead iodide perovskites, have also shown potential for multijunction perovskite solar cells because of their wide bandgap and phase stability.[6−8] Beyond solar cells, lead bromide perovskites have been used for light-emitting devices[9] and photodetectors.[10,11] For these reasons, understanding the structure−property relationships of bromine-based perovskites is fundamental to designing better optoelectronic devices. In particular, the underlying mechanisms that dominate crystallographic orientation in lead bromide perovskites are underexplored.

Solvent engineering has been used to control the crystallization kinetics and properties of perovskite polycrystalline thin films.[11−16] The highest power conversion efficiency in perovskite solar cells has been through solution processing utilizing a precursor solution of a mixture of *N*,*N*-dimethylformamide (DMF) and dimethyl sulfoxide (DMSO).[12] Differences in coordination between the solvent, DMF or DMSO, with the perovskite precursors salts (e.g., MABr, FABr, $PbBr_2$) have led to variations in the crystallization process, affecting the film morphology and crystallographic orientation.[16−18] Solvent coordination influences the formation of colloidal particles in solution, which has an important effect on the overall crystallization process and perovskite thin film morphology.[19−21] For example, adding an optimum amount of DMSO slows down crystallization and helps control crystallinity in halide perovskites.[12,14,22,23] Instead, DMF coordinates less strongly, leading to a faster and poorly controlled crystallization.[14,23] The colloids in the precursor solution may agglomerate, forming colloidal particles

Received: January 11, 2023
Revised: May 8, 2023
Published: May 25, 2023

and intermediate solvent-perovskite phases, all of which have an effect on the crystallized film.[19,20,24] In particular, iodine-based lead perovskites form numerous types of iodo-plumbate structures in solution and other solvent-perovskite phases both in DMF and DMSO.[15,18,25] Ray et al. studied and observed important differences in the precursor solution colloids leading to different final structures in Cs−Pb−Br complexes.[21]

In lead bromide perovskites, $APbBr_3$, the A site can be the inorganic Cs atom or the organic methylammonium (MA) or formamidinium (FA) molecules.[1,3−5,26] The A-site cation has also been shown to play a role in the crystallization behavior of halide perovskite thin films. For example, Petrov et al. showed that FA and MA produce different solvent-halo-plumbate complexes. For the Br-based compositions, they showed that the combination of MABr and $PbBr_2$ in DMF or DMSO did not form any solvent intermediate phase as it converted directly into $MAPbBr_3$ perovskite.[18] However, in the case of FA, combining FABr and $PbBr_2$ in DMSO, a solvent intermediate phase $(FA)_2PbBr_4$-DMSO was formed.[11,18] This suggests that the A-site cation has a very strong influence on the crystallization of thin films. An et al. studied the Cs-FA iodide-bromide compositional space from a pure DMSO precursor solution, showing that the film becomes more oriented when Cs and Br were added.[27] In agreement with An, Steele et al.[26] studied the crystallographic orientation of all-inorganic lead iodide perovskites, where they found that incorporating Br into $CsPbI_3$ reduced the orthorhombic lattice distortion and led to energetically favored preferred crystallographic orientation. Zheng et al.[3] manipulated the crystallographic orientation of lead halide perovskites by incorporating alkali metal cations such as Cs and Rb into the A-site. These different studies have shown that both solvent and composition will influence the orientation. Further, separating the solvent and composition (A-site cation) effects is important to understand the dominating factors that lead to a high degree of orientation for an optimal material design.

Herein, we investigate the role of the solvent and of the organic A-site cation on controlling crystallographic orientation in lead bromide perovskites. To understand polycrystalline film orientation, we start from the early stages of crystallization by analyzing the precursor solutions through small-angle X-ray scattering (SAXS). We study the two organic cations MA and FA, both in DMF and DMSO, to unravel the A-site cation effect on orientation. Crystallographic film orientation is analyzed by grazing-incidence wide-angle X-ray scattering (GIWAXS). We observe an interplay between solvent and A-site cation that dominates the crystallographic orientation in lead bromide perovskites. We observe that DMSO creates a highly oriented film, compared to a more random orientation, when using DMF. For the A-site cation, regardless of the solvent, $MAPbBr_3$ shows a higher degree of orientation than $FAPbBr_3$. By calculating the surface energy of the (100) and (110) plane facets, we see that $MAPbBr_3$ is thermodynamically favored to have the (100) planes oriented parallel to the surface; instead, $FAPbBr_3$ exhibits a near degeneracy between the (100) and (110) facets, leading to a lower degree of preferred orientation. In addition, we show that the A-site cation, given differences in preferred orientation, does not affect ionic diffusion but does change the ionic density as a function of a bias, as shown in impedance spectroscopy. The latter causes increased hysteresis in solar cells. Our findings provide valuable guidelines for designing lead bromide perovskites with an optimum degree of preferred crystallographic orientation for optimal performance.

METHODOLOGY

Experimental Section. *Perovskite Precursor Solution.* We prepared a 1.24 M A-$PbBr_3$ perovskite precursor solution with A being MA or FA by mixing MABr (Dyenamo, 99.99%) or FABr (Dyenamo, 99.99%) with $PbBr_2$ (TCI, 99.99% purity). The stoichiometry of the solution had a 5% molar excess of the organic cation. The solvent used was DMF (Sigma, anhydrous 99.80%), DMSO (Sigma, anhydrous 99.80%), or a volume ratio of 4:1 DMF to DMSO. The solution was stirred for 1 h at 600 rpm before deposition in a nitrogen glovebox. The solution was kept in nitrogen before any characterization at room temperature. Pb-containing solutions are hazardous; therefore, we properly sealed the solutions in glass vials and handled them with butyl gloves inside the glovebox.

Perovskite Thin Film Deposition. The lead bromide perovskite precursor solution (80 μL) was spin-coated statically on an indium-doped tin oxide (ITO)/glass or glass substrate in a two-step program: first at 1000 rpm for 10 s (acceleration of 1000 rpm/s) and then at 6000 rpm for 20 s (acceleration of 2000 rpm/s). During the spin-coating process, 250 μL of chlorobenzene (CB, Sigma 99.50%) was added dynamically. For the perovskites in DMF, CB was added 15 s after the start of the spinning process, whereas for perovskites in DMSO, CB was added at 25 s. After deposition of the perovskite solution, the substrates were annealed at 100 °C for 30 min in a nitrogen glovebox.

Perovskite Solar Cells. The solar cells fabricated were of n-i-p architecture: fluorine-doped tin oxide (FTO)/compact TiO_2/mesoporous TiO_2/lead bromide perovskite/2,2′,7,7′-tetrakis(*N*,*N*-di-*p*-methozyphenyl-amine)9,9′-spirobifluorene (Spiro-OMeTAD)/Au. The compact TiO_2 was deposited by spray pyrolysis, the mesoporous TiO_2 by spin-coating, the Spiro-OMeTAD by spin-coating, and the Au by thermal evaporation. The experimental details of deposition and fabrication are found in our previous work.[1]

Theoretical Calculations. The surface energies, γ, of $FAPbBr_3$ and $MAPbBr_3$ with different surface orientations were calculated using the following definition:

$$\gamma = \frac{(E_{slab} - NE_{bulk})}{2A} \quad (1)$$

where E_{slab} is the total energy the slab, E_{bulk} is the energy of a unit cell in the bulk of the film, N is the number of formula units within the slab, and A is the area of the surface. A slab is given by a finite number of layers of the material system that are fully periodic in x and y and isolated from a periodic image in the z direction by a vacuum gap. E_{slab} and E_{bulk} were computed with periodic DFT using Quantum Espresso.[28,29] Pseudopotentials were given by the projector-augmented wave (PAW) method and used with the Perdew−Burke−Ernzerhof functional in the generalized gradient approximation. The kinetic energy cutoff for the wavefunction was set to 80 Ry, and a corresponding energy cutoff for the charge density was set to 800 Ry. A Monkhorst−Pack k-point grids of 4 × 4 × 4 and 4 × 4 × 1 were chosen for the Brillouin zone sampling of the bulk and the slab calculations, respectively. The super-cell for the bulk calculation consisted of a single unit cell. Variable cell optimization was performed on each bulk unit cell prior to

https://doi.org/10.1021/acs.chemmater.3c00075
Chem. Mater. 2023, 35, 4181−4191

the surface construction. Each supercell for the surface calculations was constructed with a 30 Å thick slab and 15 Å vacuum gap. A geometry optimization with a fixed cell volume and shape was performed for each slab. All slabs were constructed with a complete number of perovskite formula units, resulting in two different terminations for the bottom and top surfaces. The surface energy for each termination was computed by freezing one of the surfaces in accordance with the procedure described previously.[30] One surface layer of the inorganic substructure composed of 1 Pb and 3 Br atoms was frozen in each slab, while the nuclei of the opposing surface were allowed to relax freely. All cations were set to rotate freely to account for the presence of the variety of cation orientations in the structure and its mobile nature. Due to the asymmetry introduced by the cation structure to the unit cell, cation orientation relative to the inorganic lattice and the surface was shown to break the degeneracy within a single family of plains.[30] In this study, we use the lowest energy surfaces as representative structures of the {100} and {110} families of planes. The chosen cation orientations also agree with the structures reported in the literature.[30,31] The converged geometries for each surface calculation are provided in the Supporting Information (SI).

Characterization. *SAXS.* The SAXS measurements were performed on lead bromide solutions using the HZB ASAXS instrument[32] installed at the four-crystal monochromator beamline (FCM) of the Physikalisch-Technische Bundesanstalt (PTB)[33] and operated at the BESSYII synchrotron of Helmholtz-Zentrum Berlin für Materialien und Energie (HZB). The solutions were measured in transmission in flat rectangle-shaped capillaries of 0.1 mm thickness under vacuum conditions using monochromatic X rays of 10 keV. We used a four-crystal monochromator with Si 111 crystals. This energy was optimized for the sample's transmission and scattering vector range. Data were collected three times for each sample with 600 s illumination per image. The images did not show any notable differences, implying that the solutions were stable under the chosen conditions. The 2D scattering patterns were azimuthally integrated and corrected for instrumental background and contributions of the sample holder through the BerSAS software.[34]

GIWAXS. The GIWAXS measurements were performed at the beamline for Complex Materials Scattering (11-BM) at the Brookhaven National Laboratory. The perovskite films for GIWAXS characterization were deposited on ITO/glass. An X-ray beam (13.5 keV, λ = 0.918 Å) with a footprint of 0.2 mm (height) × 0.05 mm (width) was irradiated on samples in vacuum (~10^{-5} torr) for 10 s with an incidence angle of 0.5°. Beam divergence was 1 mrad and energy resolution 0.7%. The data were analyzed using the SciAnalysis package provided by the beamline.

Photovoltaic Performance. The current density−voltage (J−V) characteristics of the solar cells were measured using a LITOS LITE setup (Fluxim, Switzerland), equipped with a Wavelabs Sinus-70 AAA solar simulator with standard AM1.5 G illumination at room temperature and ambient air. The J−V curves were obtained by scanning voltage in the range from 1.4 to −0.5 V with a scan speed of 50 mV·s^{-1} first in reverse and then in forward scan directions. The active area of the device was 0.128 cm^2, and a black metal mask with an aperture area of 0.0625 cm^2 was used to define the illuminated area.

Impedance Spectroscopy (IS). IS was carried out using a PAIOS hardware (Fluxim, Switzerland) on complete solar cells at room temperature under one sun illumination and in ambient air. The measurements were performed at five different offset voltages spaced from 0 V to the open circuit. The sweep frequency was varied from 10 MHz to 0.1 Hz, with an amplitude of 10.0 mV. Z-view software was employed to analyze the results and fit the data to the equivalent circuit.

RESULTS AND DISCUSSION

Early Stages of Crystallization. To analyze the perovskite precursor solutions, we measured SAXS of MABr-$PbBr_2$ and FABr-$PbBr_2$ precursors in DMF and DMSO (1 M). SAXS is a technique widely used to analyze the structure of nanoparticles in solution and their colloidal properties and reveals information about size, distribution, and the interaction of the particles.[20,35] Flatken et al. introduced SAXS as a technique to reveal the colloidal nature of lead halide perovskites.[20] Moreover, SAXS allows for the analysis of high concentration solutions in comparison to other techniques such as dynamic light scattering (DLS) and UV−VIS spectroscopy, which require lower concentrations.[19,20,36] Figure 1 shows SAXS

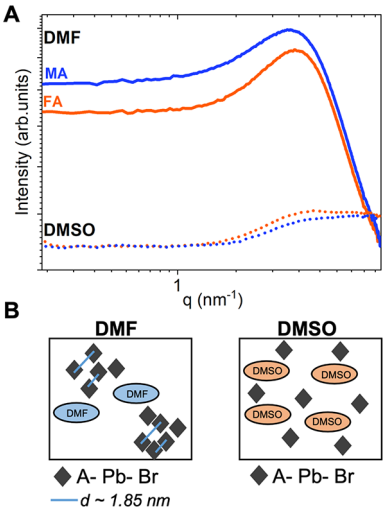

Figure 1. Particle interactions in the precursor solution. (A) SAXS data of the four studied systems $MAPbBr_3$ in DMF or DMSO and $FAPbBr_3$ in DMF or DMSO. (B) Schematic of the particle interaction in DMF and DMSO interpreted from SAXS data, A is MA or FA, and d is the interparticle distance.

results and interpretation. In Figure 1A, the DMF solutions generate clear and strong scattering peaks. In SAXS patterns, the scattering intensity indicates the presence of particles in solution. In addition, the scattering peak maximum results from particle interactions in solution.[20] This strong particle interaction indicates a quasi-crystalline prearrangement of particles in solution, which will affect the early stages of crystallization.[20,37] The maximum peak position at q_{max} reveals the mean d spacing from Bragg's law $d = 2\pi/q_{max}$. The d spacing is the distance between the mass centers of interacting colloidal particles. From Figure 1A, we calculate the q_{max} from a Lorentzian fitting and retrieve the d spacing (fitting in Figure S1). For both A-site cations in DMF, there is colloidal particle interaction in solution. The calculated interparticle distance for both FA and MA particles is around 1.85 nm. Flatken et al. have shown a similar SAXS peak when preparing different lead iodide perovskites such as $MAPbI_3$ and $FAPbI_3$ in a mixture of DMF and DMSO.[20,24] However, the pure DMSO precursor

https://doi.org/10.1021/acs.chemmater.3c00075
Chem. Mater. 2023, 35, 4181−4191

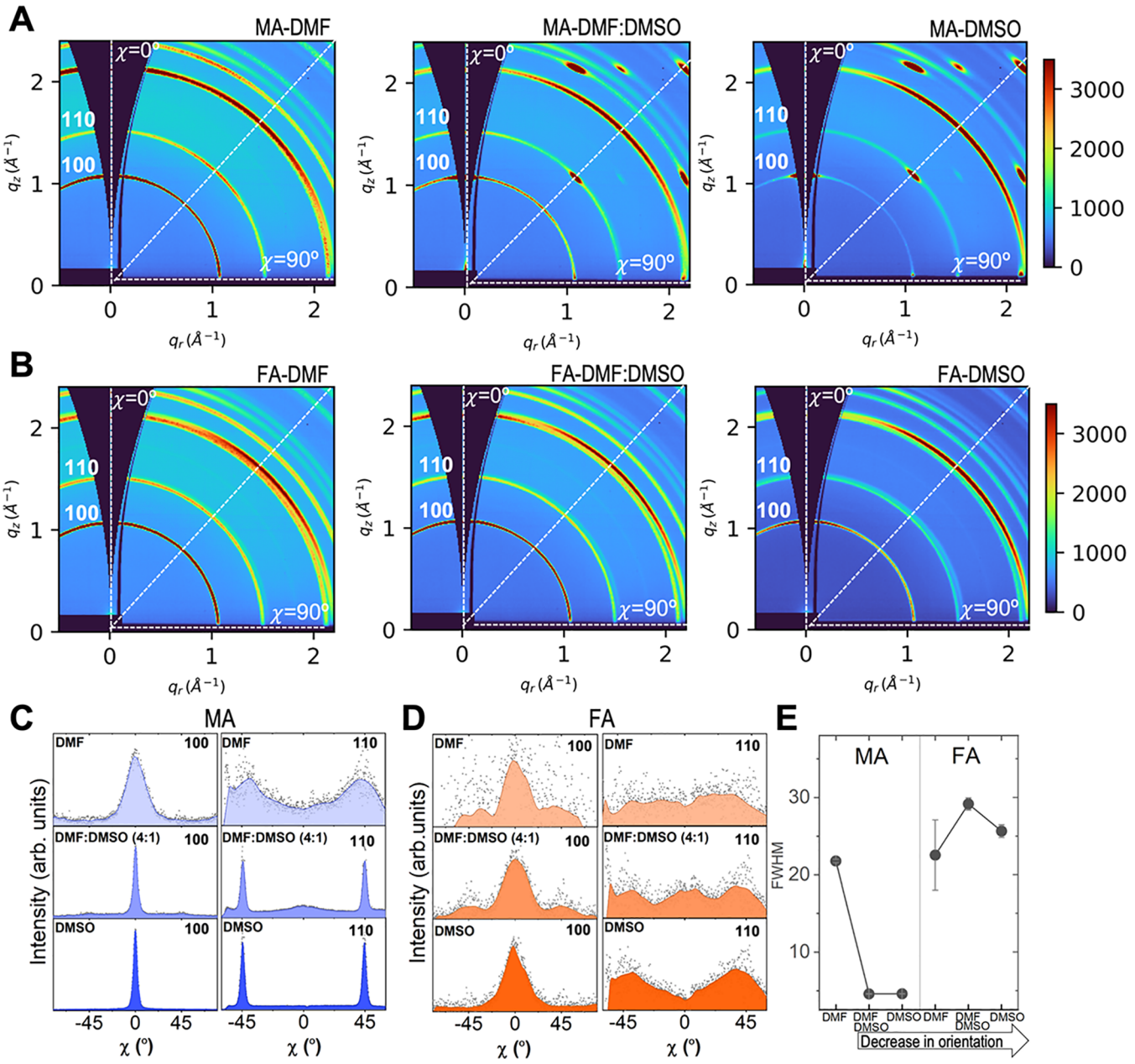

Figure 2. Interplay of solvent and A-site cation in the crystallographic orientation of lead bromide films studied by GIWAXS. (A, B) 2D GIWAXS patterns in DMF, DMF:DMSO (4:1 volume), and DMSO for (A) $MAPbBr_3$ and (B) $FAPbBr_3$. (C, D) Azimuthal integration profiles of the main Debye−Scherrer rings (100 and 110) as a function of the χ angle from GIWAXS for three solvent systems for (C) $MAPbBr_3$ and (D) $FAPbBr_3$. (E) FWHM and error bar of the 100 azimuthal peak for $MAPbBr_3$ and $FAPbBr_3$ as a function of the solvent.

solution did not show a clear scattering peak (Figure 1A). In comparison to DMF, DMSO prevents the A−Pb−Br interaction as DMSO binds more strongly than DMF to the precursor salts, preventing the A−Pb−Br interaction. This suggests that there is no colloidal particle interaction. In contrast, in DMF, a solvent with weaker coordination, the colloidal particles interact with each other and form clusters.[16] This is in agreement with the previous work by Ray et al., which showed that due to the strong coordination of DMSO, the particles in solution do not interact with each other, remaining isolated.[21] Their work also showed that DMSO forms colloidal particles one order of magnitude smaller than in DMF.[21] The schematics in Figure 1B show the hypothesized differences in particle interaction for DMF and DMSO. The shape and composition of these particles are unknown but based on the work of Ray et al.[21] and Flatken et al.,[24] we speculate that these are bromo-plumbate octahedra, the result of the interaction between A−Pb−Br in solution. We observe that in the bromine-based precursor solution, like in iodine-based perovskites,[14,16] the colloidal particle interactions in solution are driven by the solvent, while the A-site cation does not appear to play a role in the colloidal interactions.

Preferred Crystallographic Orientation. We performed GIWAXS measurements on thin films prepared with DMF and DMSO to examine the effect of different cluster formations arising from the different solvents on the orientation of the thin films. Synchrotron-based GIWAXS has been widely used to analyze the crystallographic orientation and the structure of

https://doi.org/10.1021/acs.chemmater.3c00075
Chem. Mater. 2023, 35, 4181−4191

the lead halide perovskites in thin films and solar cells.[26,38] First, we study the effect of the solvent of the precursor solution on the crystal phases and crystallographic orientation by comparing the deposition of $FAPbBr_3$ and $MAPbBr_3$ in DMF, DMF:DMSO (4:1 volume), and DMSO. The 2D GIWAXS patterns were integrated to provide 1D diffraction patterns that are shown in Figure S2. For all the solvents, $MAPbBr_3$[39] and $FAPbBr_3$[40,41] display diffraction peaks corresponding to a cubic symmetry $Pm\bar{3}m$. To identify crystallographic orientations, we analyzed the Debye−Scherrer rings from the GIWAXS patterns in Figure 2. Figure 2A shows the 2D GIWAXS for $MAPbBr_3$. As we change the solvent from DMF to DMSO, we see a clear evolution of the crystallographic orientation. For DMF, we observe a complete Debye−Scherrer ring of the (100) plane at $q_r \sim 1.06 \pm 0.06$ Å^{-1}, which indicates random orientation as the crystallographic domains scatter X-rays in all angles. The complete ring sharpens into an arc when adding one-fourth of the volume of DMSO, showing a preferred orientation of the crystallographic domains. For pure DMSO, the arc of the (100) plane sharpens further into a high-intensity Bragg spot, indicating a high degree of preferred orientation. Figure 2B shows the 2D GIWAXS for $FAPbBr_3$, where the evolution and degree of orientation differ. For DMF and DMF:DMSO, $FAPbBr_3$ shows a uniform intensity in all the rings, suggesting that the film has no preferred orientation. For pure DMSO, the ring of the (100) plane sharpens into an arc with maximum intensity at $q_r = 0$, indicating an increase in the degree of preferred crystallographic orientation from random to preferentially oriented crystallographic domains.

To further analyze and quantify crystallographic orientation, we integrated the azimuthal profile (χ) of the Debye−Scherrer rings of the first two peaks corresponding to the (100) plane at $q_r \sim 1.06 \pm 0.06$ Å^{-1} and the (110) plane at $q_r \sim 1.4 \pm 0.06$ Å^{-1}. The peak of the azimuthal profile provides information about the direction of the preferred orientation of the planes. Since the grazing-incidence measurements give rise to a missing wedge near the q_z axis due to the curvature of the Ewald sphere, it is important to analyze the orientation of the two planes. We studied the (100) and (110) planes, where the (110) plane complements the quantitative description of orientation. The (100) and (110) Debye−Scherrer rings are integrated from $\chi = -80°$ to 80°, where $\chi = 0°$ is set at $q_r = 0$ (out-of-plane) and $\chi = 90°$ at $q_z = 0$ (in-plane). For $MAPbBr_3$, we integrated the azimuthal profile of the Debye−Scherrer rings from Figure 2A into Figure 2C, and for $FAPbBr_3$, the azimuthal profiles are integrated from Figure 2B into Figure 2D. To understand the dispersion in the preferred orientation of the crystallographic domains, we fit the azimuthal profile peaks into a pseudo-Voigt or Gaussian function from which we obtain the full width at half-maximum (FWHM) and other statistical parameters shown in Table S1. The azimuthal profile for $MAPbBr_3$ in Figure 2C shows a peak at 0° of the (100) plane, evidence that these planes are oriented parallel to the substrate. In addition, the azimuthal profile peak of the (110) plane is around 45°, which is consistent with the (100) plane being oriented parallel to the substrate (explanation in Figure S3). We also observe that the choice of solvent changes the FWHM of the fitted azimuthal peak, as expected from the evolution in the degree of orientation seen in the 2D GIWAXS patterns in Figure 2A. In $MAPbBr_3$ in DMF, the (100) peak is broader, and the fitting has a larger error and low R^2 (Table S1). When DMSO is added (DMF:DMSO and pure DMSO), the azimuthal peaks sharpen, and the raw data fits nicely into the pseudo-Voigt function with a high R^2 (Table S1). The sharp azimuthal profile peaks indicate a high degree of preferred orientation of the (100) plane parallel to the substrate. In addition, the $MAPbBr_3$ from DMSO has the lowest FWHM, hence the highest degree of preferred orientation.

In Figure 2D, we plot the azimuthal profile peaks for $FAPbBr_3$. Compared to $MAPbBr_3$, the $FAPbBr_3$ peaks are all broader and have a higher FWHM, showing a lower degree of preferred orientation. For DMF, the crystallographic domains show dispersion in the integrated data, suggesting a low degree of preferred orientation. The fitted Gaussian peak for DMF has a very low R^2 and large error in Table S1. The poor fitting for $FAPbBr_3$-DMF is attributed to the random orientation of the film. As we added DMSO to the precursor solution, the R^2 of the fit of the (100) azimuthal peak 0° increased, showing a preferred orientation of crystallographic domains with the (100) plane parallel to the substrate. For $FAPbBr_3$-DMF:DMSO, the (110) azimuthal profile shows three broad peaks at around ± 45° and 0°, which indicates a lower degree of orientation and a higher dispersion. With pure DMSO, the (100) azimuthal peak sharpens, the (110) azimuthal profile shows two broad peaks at ± 45°, and the data fitting improves, with a higher R^2 and lower error in Table S1. These changes suggest that pure DMSO induces some preferred orientation, even in FA-based films. These results on preferred crystallographic orientation were corroborated by comparing the ratio in intensity between the 100 and 110 peaks from Bragg Brentano XRD to complement the missing wedge from GIWAXS (Figure S4). The FWHM of the (100) azimuthal peak shown in Figure 2E quantifies the dispersion of orientation of the crystallographic domains. $MAPbBr_3$ films deposited from a pure DMSO precursor solution show the lowest FWHM, evidence of the highest degree of preferred orientation. In contrast, $FAPbBr_3$ shows a higher FWHM, decreasing the degree of preferred orientation. Additionally, we verified that the preferred orientation was induced by the solvent and was not kinetically determined by the antisolvent addition times. Figures S5 and S6 show the GIWAXS patterns and azimuthal integration of lead bromide perovskite films adding CB as antisolvent at different times during the spin-coating process.

The SAXS results discussed in the previous section suggest that there are interactions between the bromo-plumbate octahedra colloidal particles in DMF, which favor the possible formation of agglomerates in solution. We speculate that these colloidal aggregates could form dispersed and agglomerated nuclei for the crystallization process. This could lead to the random orientation observed in DMF from the GIWAXS measurements, as illustrated in the schematics of Figure S7. The higher degree of random orientation in DMF is observed regardless of the cation type, indicative of this solvent-dominated phenomenon. To further understand the origins of preferred crystallographic orientation in lead bromide perovskites, we now discuss why MA and FA impact preferred orientation in pure DMSO, where there are no colloidal interactions. Instead, in DMSO, the octahedra particles and nuclei would be isolated, and the crystallization is slowed down. We also learned from SAXS in Figure 1 that there were no differences between MA and FA in solution. However, the crystallized films in pure DMSO still show differences in orientation when comparing $MAPbBr_3$ and $FAPbBr_3$. For this reason, other underlying forces and mechanisms must lead to

https://doi.org/10.1021/acs.chemmater.3c00075
Chem. Mater. 2023, 35, 4181−4191

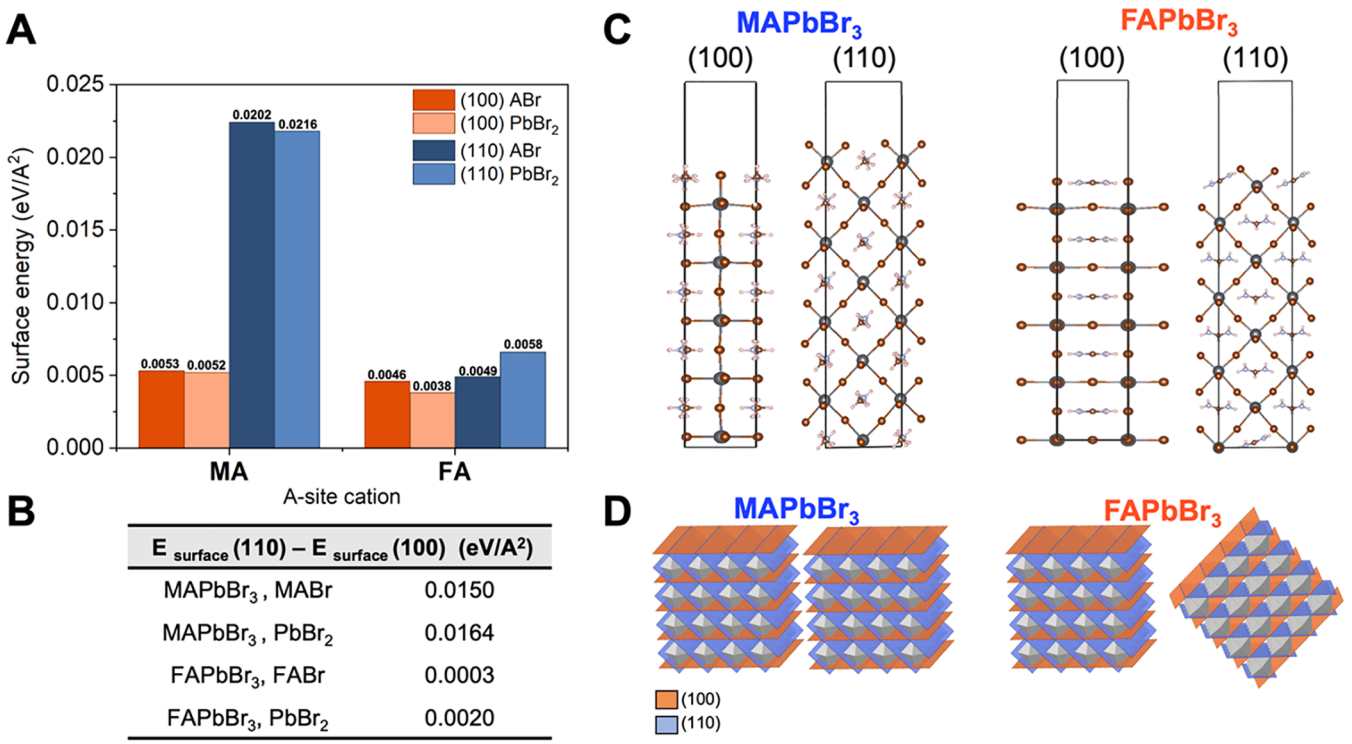

$E_{surface}(110) - E_{surface}(100)$ (eV/A²)	
$MAPbBr_3$, MABr	0.0150
$MAPbBr_3$, $PbBr_2$	0.0164
$FAPbBr_3$, FABr	0.0003
$FAPbBr_3$, $PbBr_2$	0.0020

Figure 3. Results of the DFT calculation for the representative (100) and (110) surfaces of $MAPbBr_3$ and $FAPbBr_3$. (A) Surface energy of the analyzed structures computed for surfaces with $PbBr_2$ or FABr/MABr termination. (B) Energy difference between the corresponding (110) and (100) surfaces. (C) Representative final structures of the FABr/MABr-terminated calculation for $MAPbBr_3$ and $FAPbBr_3$. The inorganic lattice of the bottom surface demonstrates the $PbBr_2$ phase was frozen throughout the calculation. (D) Pictorial representation of the increased surface disorder due to the presence of two competing surfaces in $FAPbBr_3$.

these differences in orientation for the different A-site cations in lead bromide perovskites.

Mechanisms for Preferred Orientation. We used periodic DFT to calculate the relative surface energies for $MAPbBr_3$ and $FAPbBr_3$ to help explain the difference in crystallographic orientation observed in the GIWAXS measurements arising from the difference in A-site cation. The calculated surface energies for a representative surface from the {100} and {110} family of planes are presented in Figure 3A. We considered both $PbBr_2$ and FABr/MABr termination, but we observed that the termination only leads to a qualitatively negligible variation in the surface energy regardless of A-site cation and surface plane. Therefore, the following qualitative conclusions are discussed regardless of this distinction.

Figure 3A shows that the (100)-terminated slab is energetically more stable in comparison to the (110)-terminated slab for $MAPbBr_3$, in agreement with previous calculations. The (100) and (110) $FAPbBr_3$ have almost equivalent surface energies. The energy differences between the (110) and (100) surfaces for both cations are presented in Figure 3B. The large energy difference for MA compared to FA agrees with and helps explain the experimentally observed difference in crystallographic orientation. For MA, the (100) surface is energetically more stable and will therefore be the dominant surface that is formed. For FA, the relative degeneracy between the (100) and (110) surfaces implies no thermodynamic driving force to form one surface over the other. Therefore, both surfaces can be easily formed, leading to a higher degree of orientational disorder.

The relative difference in surface energies between the $MAPbBr_3$ and $FAPbBr_3$ surface can be understood by comparing the orientation of the A-site cation in the final surface structures (Figure 3C) to that in the bulk. In all cases, the organic A-site cation adopts a configuration where its dipole moment is parallel to the surface to minimize the energetic penalty of forming the surface. The difference is that in $MAPbBr_3$, the orientation of the A-site cation in the bulk already corresponds to a planar configuration; $MAPbBr_3$ only exhibits a minor geometric reorganization for both the (100) and (110) surfaces in comparison to the bulk structure associated with a rotation along the C−N bond for the MA cation. Similarly, the FA cation is already planar in the (100) surface and therefore does not reorient significantly. However, the bulk configuration of the FA cation is perpendicular to the (110) surface plane. Therefore, the FA cations close to the surface significantly reorient upon the formation of the (100) surface, such that they adopt a configuration parallel to the (100) surface. This reorientation leads to an energetic stabilization of the (100) surface and results in the relative energy degeneracy between the (100) and (110) terminations. This planar configuration of the FA cation has been previously observed in the context of $FAPbI_3$.[42] While this analysis does not account for the kinetics of surface formation, the presence of two competing surface orientations in $FAPbBr_3$ provides thermodynamic insight into the increased disorder observed in the GIWAXS measurements (Figure 3D).

Solar Cell Performance and Ionic Movement. Having understood the effect of the A-site cation on preferred crystallographic orientation, we studied how the choice of A-site cation impacts the electric response in perovskite solar

https://doi.org/10.1021/acs.chemmater.3c00075
Chem. Mater. 2023, 35, 4181−4191

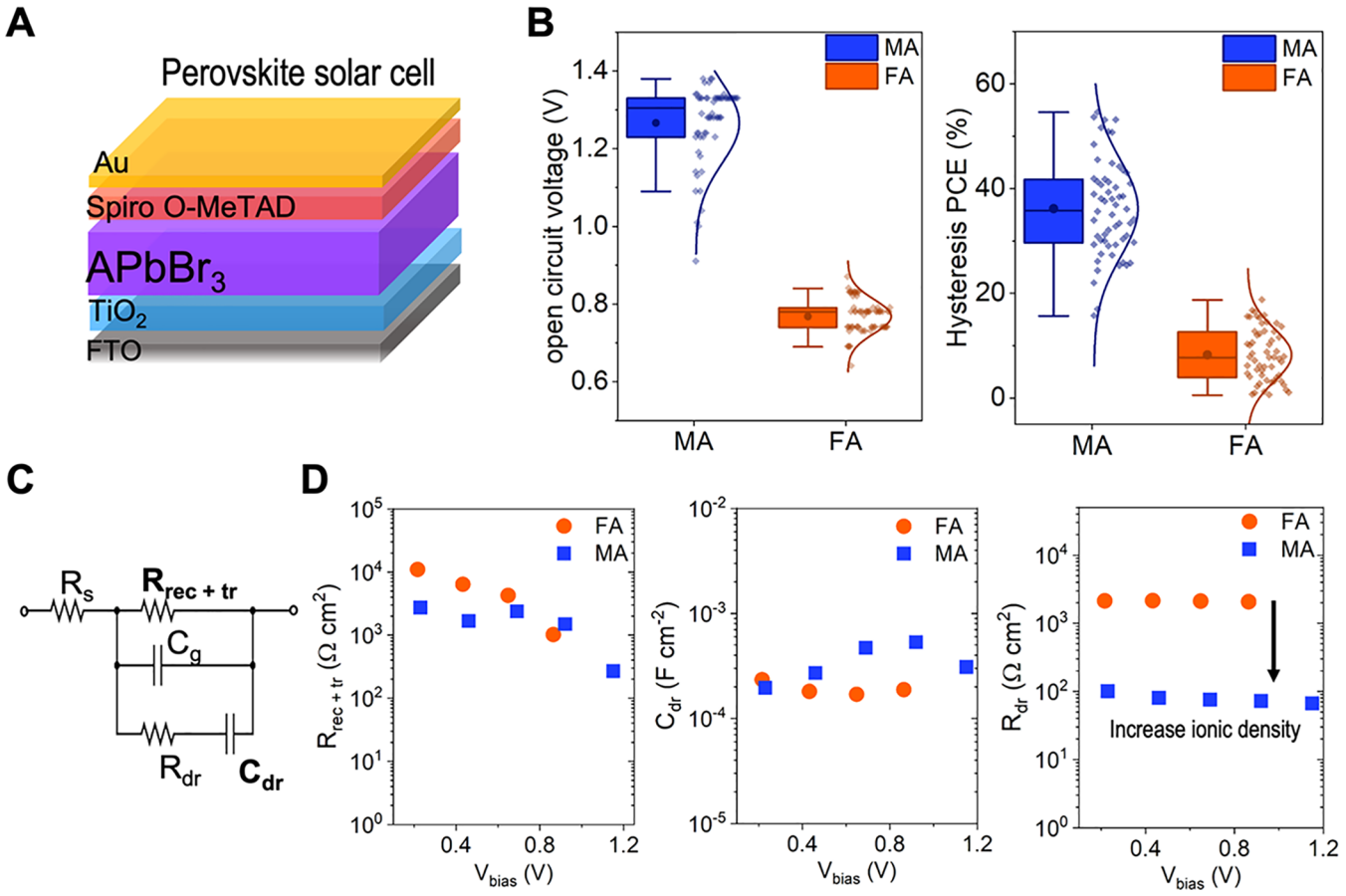

Figure 4. Electrical properties of the solar cell. (A) Schematic of a perovskite solar cell architecture where A in $APbBr_3$ is MA or FA. (B) Box plots of the solar cell characterization from the $J-V$ curve open circuit voltage, and absolute hysteresis index of the power conversion efficiency (PCE). (C, D) Impedance spectroscopy measurements for $MAPbBr_3$ and $FAPbBr_3$ solar cells. (C) Equivalent circuit used for the analysis of the impedance spectra. (D) Recombination and transport resistance for different applied biases (R_{rec+tr}), low-frequency capacitance for different applied biases (C_{dr}), and low-frequency resistor (R_{dr}).

cells. We confirmed the same differences in the preferred orientation of the MA and FA lead bromide perovskites on the solar cell substrate (Figure S8). The solar cells had an n-i-p architecture that is described in the experimental section, and is shown schematically in Figure 4A. Lead bromide perovskite solar cells exhibit significantly lower efficiency compared to their iodine counterparts due to their wider bandgap and unoptimized contacts.[43−45] However, their large bandgap expands the scope of application into multijunction solar cells or other optoelectronic applications. We measured the $J-V$ characteristics of the solar cells under simulated solar illumination (AM 1.5 G, 100 mW/cm^2) to calculate the figures of merit of the solar cells ($J-V$ curves example in Figure S9). We measured the open circuit voltage, short circuit current, fill factor, power conversion efficiency (PCE) from the $J-V$ scan, and the stabilized PCE from the maximum power point tracking (PCE_{MPPT}). The statistical distribution of the open circuit voltage is shown in Figure 4B. The optical bandgap variations (Figure S10) dominate the trends in the open circuit voltage. A larger bandgap for MA relative to FA increases the open circuit voltage and decreases the short circuit current (Figure S11). Given the differences in the bandgap, we cannot attribute the differences in charge carrier transport solely to crystallographic orientation. However, based on previous studies, a better charge carrier transport is expected for an oriented polycrystalline thin film.[1,3] The other figures of merit of the solar cells, fill factor, and PCE from the reverse scan are reported in the SI (Figure S11).

Beyond the effect of crystallographic orientation on charge carrier transport in perovskite solar cells, some studies have shown that orientation can influence the pathway of ionic movement. It has been suggested that the halide and Pb ions can move along the (110) plane.[2] Hysteresis of the $J-V$ curve in lead halide perovskite solar cells has been attributed to ion migration,[46] among others.[47−49] Although ionic movement is not solely associated with $J-V$ curve hysteresis,[50] we analyze the hysteresis behavior to get an insight into how crystallographic orientation influences ion migration. Therefore, we calculated the absolute hysteresis index from the PCE to study the effects of ionic movement by comparing the difference between the forward scan (FS) and reverse scan (RS) of the PCE as follows:[51]

$$\text{hysteresis\%} = \frac{|PCE_{RS} - PCE_{FS}|}{PCE_{RS}} \quad (2)$$

The devices made with $FAPbBr_3$ perovskites show a lower hysteresis than those made with $MAPbBr_3$. The hysteresis behavior associated with ion migration that is dependent on lead halide perovskite composition is in line with the previous reports.[47,49,52] In $MAPbBr_3$, the defect activation energy barrier for ion movement has been calculated to be lower than that of $FAPbBr_3$, giving rise to more ionic movement, and explaining

https://doi.org/10.1021/acs.chemmater.3c00075
Chem. Mater. 2023, 35, 4181−4191

the larger hysteresis behavior for $MAPbBr_3$.[52] In addition, the hydrogen bond between the organic A-site cation and the bromine is stronger for FA than MA, limiting the motion of the cation in the case of $FAPbBr_3$.[52] This could be an additional explanation for the increase in hysteresis in $MAPbBr_3$ solar cells.

To further understand the role of A-site cation on ionic motion in these materials, we measured impedance spectroscopy under different biases. The resulting Nyquist plots reproduce the characteristic patterns of lead halide perovskite solar cells[53] (see representative spectra in Figure S12). The Nyquist plots were fitted to an equivalent circuit reported elsewhere (illustrated in Figure 4C).[54] This circuit includes a resistor (R_{rec+tr}) that couples both the recombination and transport resistances due to the low chemical capacitance of perovskite solar cells and a low-frequency branch with a capacitor (C_{dr}) and resistor (R_{dr}), both related to the ionic nature of the lead halide perovskites. In Figure 4D, R_{rec+tr} displays negligible variations between $MAPbBr_3$ and $FAPbBr_3$ under lower bias values.

High capacitance values at low-frequency regimes have been a fingerprint of lead halide perovskite solar cells.[54] The origin of this low-frequency capacitance is typically attributed to the mixed ionic-electronic nature of these materials.[53,55] In the equivalent circuit employed to analyze the results, this capacitance is modeled by a constant phase element C_{dr} to account for dispersive phenomena, yet with exponent values close to 1. The C_{dr} can be interpreted as an indication of increased ionic density or as higher ionic diffusion.[56] Therefore, a comparative analysis of the C_{dr} is used to understand the ionic differences between $MAPbBr_3$ and $FAPbBr_3$, as observed in Figure 4D. FA has a slightly lower C_{dr} than MA. The slight reduction of C_{dr} can be interpreted as an indication of increased ionic diffusion or higher ionic density in $FAPbBr_3$. To decouple the effects between ionic density and ionic diffusion, we examined the low-frequency part of the spectrum R_{dr}. The increase of R_{dr} for $FAPbBr_3$ compared to $MAPbBr_3$ confirms the higher ionic density of the latter. These variations are in line with the increase of the absolute $J-V$ hysteresis in $MAPbBr_3$ solar cells (Figure 4B). These experimental results align with published computational results[52] in which bromide vacancies and interstitials had much lower formation energies and higher densities in $MAPbBr_3$ than for $FAPbBr_3$, where the FA cation suppressed ion diffusion.

Analyzing the effect of preferred crystallographic orientation on the ionic effects, we observe that $MAPbBr_3$, with a high preferential orientation, has the highest ionic density compared to the randomly oriented $FAPbBr_3$. We suggest that ionic effects could be affected by the crystallographic orientation in lead bromide perovskites. Previous studies have shown the effects of in-plane crystallographic orientation of lead halide perovskites, where it has been observed that preferred orientation leads to a faster movement of ions. Fassl et al. studied the effect of in-plane crystallographic orientation on ionic transport rate from simulations and experimental work.[57] They found that the relative orientation of the crystals affects ionic migration in polycrystalline films; crystals with preferred orientation had uniform ion transport while randomly oriented crystals had varying rates of ionic transport. Further, Eames et al. showed that in perovskite films with vacancy defects,[58] the halide migrates along the octahedron edge between halide sites.[58] Given that mobile ions can move in the ⟨110⟩ family of directions, Flannery et al.[2] observed that ionic movement through the absorber layer is higher if the crystals in a mixed-halide perovskite film were highly oriented in the (110) plane. While an effect of orientation on charge transport cannot be excluded, we show that increased preferred orientation along the (100) plane does not contribute to an improved ion diffusion. Differences in the ionic contribution are ascribed to an increased ionic density in the highly ordered $MAPbBr_3$ perovskite.

CONCLUSIONS

We studied the effect of the solvent and organic A-site cation on the crystallographic orientation in lead bromide thin films. We showed that there is an interplay between the type of solvent and A-site cation that determines the preferred crystallographic orientation in bromine-based perovskites. Polycrystalline thin films prepared from solution in DMF solvent exhibit less preferred orientation, whereas films prepared from solutions in DMSO exhibit higher degree of preferred orientation for both FA and MA. Regardless of the solvent, $MAPbBr_3$ showed the highest degree of preferred orientation compared to $FAPbBr_3$. Theoretical calculations showed that $MAPbBr_3$ is energetically favored to grow along the (100) plane while in $FAPbBr_3$, the (100) and (110) surfaces are nearly degenerate in energy, and both are equally favored for growth. In addition, we observed that there are larger ionic movement effects in the highly oriented $MAPbBr_3$ solar cells. The $J-V$ hysteresis of the solar cells and impedance spectroscopy results indicate higher ionic density effects in $MAPbBr_3$. This work provides new insights on the role of both solvent and A-site cation in the crystallization of thin films, crucial for long-term stability of perovskite solar cells.

ASSOCIATED CONTENT

Supporting Information

The Supporting Information is available free of charge at https://pubs.acs.org/doi/10.1021/acs.chemmater.3c00075.

Complete experimental section with materials and methods; iodide-based results; peak assignment for the $Cs_{0.17}FA_{0.83}PbBr_3$ sample after humidity exposure; details on the azimuthal integration from GIWAXS; further SEM images and the complete optical properties values of all studied films; survey spectra and complete information on XPS; details about the TRMC setup and perovskite lifetimes; and impedance spectroscopy complete data (PDF)

Crystallographic information files for the studied compounds (ZIP)

AUTHOR INFORMATION

Corresponding Authors

Joshua S. Kretchmer − *School of Chemistry and Biochemistry, Georgia Institute of Technology, Atlanta, Georgia 30332, United States;* orcid.org/0000-0003-3468-0481; Email: jkretchmer@gatech.edu

Juan-Pablo Correa-Baena − *School of Materials Science and Engineering, Georgia Institute of Technology, Atlanta, Georgia 30332, United States;* orcid.org/0000-0002-3860-1149; Email: jpcorrea@gatech.edu

https://doi.org/10.1021/acs.chemmater.3c00075
Chem. Mater. 2023, 35, 4181−4191

Authors

Juanita Hidalgo − *School of Materials Science and Engineering, Georgia Institute of Technology, Atlanta, Georgia 30332, United States*

Yu An − *School of Materials Science and Engineering, Georgia Institute of Technology, Atlanta, Georgia 30332, United States;* orcid.org/0000-0002-1382-5293

Dariia Yehorova − *School of Chemistry and Biochemistry, Georgia Institute of Technology, Atlanta, Georgia 30332, United States*

Ruipeng Li − *National Synchrotron Light Source II, Brookhaven National Lab, Upton, New York 11973, United States*

Joachim Breternitz − *Department of Structure and Dynamics of Energy Materials, Helmholtz Zentrum Berlin für Materialien und Energie, 14109 Berlin, Germany;* orcid.org/0000-0002-0192-6919

Carlo A.R. Perini − *School of Materials Science and Engineering, Georgia Institute of Technology, Atlanta, Georgia 30332, United States*

Armin Hoell − *Department of Structure and Dynamics of Energy Materials, Helmholtz Zentrum Berlin für Materialien und Energie, 14109 Berlin, Germany;* orcid.org/0000-0002-7080-8393

Pablo P. Boix − *Institut de Ciència dels Materials, Universidad de València, Paterna 46980 Valencia, Spain;* orcid.org/0000-0001-9518-7549

Susan Schorr − *Department of Structure and Dynamics of Energy Materials, Helmholtz Zentrum Berlin für Materialien und Energie, 14109 Berlin, Germany; Freie Universitaet Berlin, Institute of Geological Sciences, 12249 Berlin, Germany*

Complete contact information is available at: https://pubs.acs.org/10.1021/acs.chemmater.3c00075

Author Contributions

J.H. formulated the project and wrote the manuscript, fabricated thin films and solar cells, performed and analyzed the GIWAXS experiments, and performed IS measurements on solar cells. Y.A. helped formulate the project, fabricated thin films and solar cells, and performed UV−Vis, PL, and general data analysis. D.Y. helped in the analysis of the data and performed and analyzed the computational work. R.L. performed GIWAXS data collection and analysis at BNL. A.H. performed the SAXS experiments and the data reduction. C.A.R.P. assisted in the analysis, writing, and review of the whole manuscript. J.B. performed SAXS data collection and analysis at BESSY. S.S. oversaw and analyzed the SAXS data and revised all the manuscript. P.B. analyzed and interpreted all the IS data. J.S.K. supervised the computational work and participated in the whole data analysis of the manuscript. J.P.C.B. supervised the entire work and helped in analysis, manuscript writing, and revision. All the authors have read, corrected, and agreed with the manuscript.

Notes

The authors declare no competing financial interest.

■ ACKNOWLEDGMENTS

This work was performed in part in the Georgia Tech Institute for Electronics and Nanotechnology, a member of the National Nanotechnology Coordinated Infrastructure (NNCI), which is supported by the National Science Foundation (Grant ECCS-1542174). The research team benefitted from the Georgia Tech Forming Teams Seed Grant entitled "Center for Cross Transport Processes in Quantum Materials". J.H. acknowledges the Department of Education Graduate Assistance in Areas of National Need (GAANN) program at Georgia Institute of Technology (Award #P200A180075) and the Graduate Education for Minorities (GEM) fellowship for career funding. Y.A. thanks the China Scholarship Council (CSC) for financial support from fellowship No. 201906250003 and financial support from the National Science Foundation of China (No. 21676188). This research used the CMS 11-BM beamline of the National Synchrotron Light Source II, a US Department of Energy (DOE) Office Science User Facility operated for the DOE office of Science by the Brookhaven National Laboratory under Contract DE-SC0012704. J.H. and Y.A. also thank all the members of the Energy Materials Laboratory at Georgia Tech for their help and discussions about the project. J.H., J.B., A.H., and S.S. would like to thank Ana Palacios-Saura, Niyaz Huseyn-Zada, and Dr. Uwe Keiderling for assistance with the SAXS measurements. J.B., A.H., and S.S. thank the PTB (the German national metrology institute) for the ability to use the FCM beamline at BESSYII of Helmholtz-Zentrum Berlin to carry out SAXS measurements, especially Dieter Skroblin and Christian Gollwitzer for the experimental support.

■ REFERENCES

(1) Hidalgo, J.; Perini, C. A. R.; Castro-Mendez, A.-F.; Jones, D.; Köbler, H.; Lai, B.; Li, R.; Sun, S.; Abate, A.; Correa-Baena, J.-P. Moisture-Induced Crystallographic Reorientations and Effects on Charge Carrier Extraction in Metal Halide Perovskite Solar Cells. *ACS Energy Lett.* **2020**, *5*, 3526−3534.

(2) Flannery, L.; Ogle, J.; Powell, D.; Tassone, C.; Whittaker-Brooks, L. Voltage Bias Stress Effects in Metal Halide Perovskites Are Strongly Dependent on Morphology and Ion Migration Pathways. *J. Mater. Chem. A* **2020**, *8*, 25109−25119.

(3) Zheng, G.; Zhu, C.; Ma, J.; Zhang, X.; Tang, G.; Li, R.; Chen, Y.; Li, L.; Hu, J.; Hong, J.; Chen, Q.; Gao, X.; Zhou, H. Manipulation of Facet Orientation in Hybrid Perovskite Polycrystalline Films by Cation Cascade. *Nat. Commun.* **2018**, *9*, 1−11.

(4) Rivnay, J.; Mannsfeld, S. C. B.; Miller, C. E.; Salleo, A.; Toney, M. F. Quantitative Determination of Organic Semiconductor Microstructure from the Molecular to Device Scale. *Chem. Rev.* **2012**, *112*, 5488−5519.

(5) Joseph Kline, R.; McGehee, M. D.; Toney, M. F. Highly Oriented Crystals at the Buried Interface in Polythiophene Thin-Film Transistors. *Nature Mater* **2006**, *5*, 222−228.

(6) Vasileiadou, E. S.; Hadar, I.; Kepenekian, M.; Even, J.; Tu, Q.; Malliakas, C. D.; Friedrich, D.; Spanopoulos, I.; Hoffman, J. M.; Dravid, V. P.; Kanatzidis, M. G. Shedding Light on the Stability and Structure−Property Relationships of Two-Dimensional Hybrid Lead Bromide Perovskites. *Chem. Mater.* **2021**, *33*, 5085−5107.

(7) Kulbak, M.; Gupta, S.; Kedem, N.; Levine, I.; Bendikov, T.; Hodes, G.; Cahen, D. Cesium Enhances Long-Term Stability of Lead Bromide Perovskite-Based Solar Cells. *J. Phys. Chem. Lett.* **2016**, *7*, 167−172.

(8) Ijaz, P.; Imran, M.; Soares, M. M.; Tolentino, H. C. N.; Martín-García, B.; Giannini, C.; Moreels, I.; Manna, L.; Krahne, R. Composition-, Size-, and Surface Functionalization-Dependent Optical Properties of Lead Bromide Perovskite Nanocrystals. *J. Phys. Chem. Lett.* **2020**, *11*, 2079−2085.

(9) Leyden, M. R.; Meng, L.; Jiang, Y.; Ono, L. K.; Qiu, L.; Juarez-Perez, E. J.; Qin, C.; Adachi, C.; Qi, Y. Methylammonium Lead Bromide Perovskite Light-Emitting Diodes by Chemical Vapor Deposition. *J. Phys. Chem. Lett.* **2017**, *8*, 3193−3198.

(10) Gavranovic, S.; Pospisil, J.; Zmeskal, O.; Novak, V.; Vanysek, P.; Castkova, K.; Cihlar, J.; Weiter, M. Electrode Spacing as a Determinant of the Output Performance of Planar-Type Photodetectors Based on Methylammonium Lead Bromide Perovskite Single Crystals. *ACS Appl. Mater. Interfaces* **2022**, *14*, 20159−20167.
(11) Hu, C.; Shivarudraiah, S. B.; Sung, H. H. Y.; Williams, I. D.; Halpert, J. E.; Yang, S. Discovery of a New Intermediate Enables One-Step Deposition of High-Quality Perovskite Films via Solvent Engineering. *Solar RRL* **2021**, *5*, 2000712.
(12) Rezaee, E.; Zhang, W.; Silva, S. R. P. Solvent Engineering as a Vehicle for High Quality Thin Films of Perovskites and Their Device Fabrication. *Small* **2021**, *17*, 2008145.
(13) Shargaieva, O.; Näsström, H.; Smith, J. A.; Többens, D.; Munir, R.; Unger, E. Hybrid Perovskite Crystallization from Binary Solvent Mixtures: Interplay of Evaporation Rate and Binding Strength of Solvents. *Mater. Adv.* **2020**, *1*, 3314−3321.
(14) Petrov, A. A.; Sokolova, I. P.; Belich, N. A.; Peters, G. S.; Dorovatovskii, P. V.; Zubavichus, Y. V.; Khrustalev, V. N.; Petrov, A. V.; Grätzel, M.; Goodilin, E. A.; Tarasov, A. B. Crystal Structure of DMF-Intermediate Phases Uncovers the Link Between $CH_3NH_3PbI_3$ Morphology and Precursor Stoichiometry. *J. Phys. Chem. C* **2017**, *121*, 20739−20743.
(15) Soe, C. M. M.; Nie, W.; Stoumpos, C. C.; Tsai, H.; Blancon, J.-C.; Liu, F.; Even, J.; Marks, T. J.; Mohite, A. D.; Kanatzidis, M. G. Understanding Film Formation Morphology and Orientation in High Member 2D Ruddlesden−Popper Perovskites for High-Efficiency Solar Cells. *Adv. Energy Mater.* **2018**, *8*, 1700979.
(16) Hamill, J. C.; Schwartz, J.; Loo, Y.-L. Influence of Solvent Coordination on Hybrid Organic−Inorganic Perovskite Formation. *ACS Energy Lett.* **2018**, *3*, 92−97.
(17) Petrov, A. A.; Ordinartsev, A. A.; Fateev, S. A.; Goodilin, E. A.; Tarasov, A. B. Solubility of Hybrid Halide Perovskites in DMF and DMSO. *Molecules* **2021**, *26*, 7541.
(18) Petrov, A. A.; Fateev, S. A.; Khrustalev, V. N.; Li, Y.; Dorovatovskii, P. V.; Zubavichus, Y. V.; Goodilin, E. A.; Tarasov, A. B. Formamidinium Haloplumbate Intermediates: The Missing Link in a Chain of Hybrid Perovskites Crystallization. *Chem. Mater.* **2020**, *32*, 7739−7745.
(19) Dutta, N. S.; Noel, N. K.; Arnold, C. B. Crystalline Nature of Colloids in Methylammonium Lead Halide Perovskite Precursor Inks Revealed by Cryo-Electron Microscopy. *J. Phys. Chem. Lett.* **2020**, *11*, 5980−5986.
(20) Flatken, M. A.; Hoell, A.; Wendt, R.; Härk, E.; Dallmann, A.; Prause, A.; Pascual, J.; Unger, E.; Abate, A. Small-Angle Scattering to Reveal the Colloidal Nature of Halide Perovskite Precursor Solutions. *J. Mater. Chem. A* **2021**, *9*, 13477−13482.
(21) Ray, A.; Maggioni, D.; Baranov, D.; Dang, Z.; Prato, M.; Akkerman, Q. A.; Goldoni, L.; Caneva, E.; Manna, L.; Abdelhady, A. L. Green-Emitting Powders of Zero-Dimensional Cs_4PbBr_6: Delineating the Intricacies of the Synthesis and the Origin of Photoluminescence. *Chem. Mater.* **2019**, *31*, 7761−7769.
(22) Chen, B.; Yu, Z. J.; Manzoor, S.; Wang, S.; Weigand, W.; Yu, Z.; Yang, G.; Ni, Z.; Dai, Z.; Holman, Z. C.; Huang, J. Blade-Coated Perovskites on Textured Silicon for 26%-Efficient Monolithic Perovskite/Silicon Tandem Solar Cells | Elsevier Enhanced Reader. *Joule* **2020**, *4*, 850−864.
(23) Zhang, J.; Zhang, L.; Li, X.; Zhu, X.; Yu, J.; Fan, K. Binary Solvent Engineering for High-Performance Two-Dimensional Perovskite Solar Cells. *ACS Sustainable Chem. Eng.* **2019**, *7*, 3487−3495.
(24) Flatken, M. A.; Radicchi, E.; Wendt, R.; Buzanich, A. G.; Härk, E.; Pascual, J.; Mathies, F.; Shargaieva, O.; Prause, A.; Dallmann, A.; De Angelis, F.; Hoell, A.; Abate, A. Role of the Alkali Metal Cation in the Early Stages of Crystallization of Halide Perovskites. *Chem. Mater.* **2022**, *34*, 1121−1131.
(25) Keller, T.; Nickel, N. H.; Rappich, J. Competition of Iodide/Bromide Ions in the Formation of Methylammonium Lead Halide in Different Solvents. *J. Phys. Chem. C* **2022**, *126*, 17656−17662.
(26) Steele, J. A.; Solano, E.; Jin, H.; Prakasam, V.; Braeckevelt, T.; Yuan, H.; Lin, Z.; de Kloe, R.; Wang, Q.; Rogge, S. M. J.; Van Speybroeck, V.; Chernyshov, D.; Hofkens, J.; Roeffaers, M. B. J. Texture Formation in Polycrystalline Thin Films of All-Inorganic Lead Halide Perovskite. *Adv. Mater.* **2021**, *33*, 1−9.
(27) An, Y.; Perini, C. A. R.; Hidalgo, J.; Castro-Méndez, A.-F.; Vagott, J. N.; Li, R.; Saidi, W. A.; Wang, S.; Li, X.; Correa-Baena, J.-P. Identifying High-Performance and Durable Methylammonium-Free Lead Halide Perovskites *via* High-Throughput Synthesis and Characterization. *Energy Environ. Sci.* **2021**, *14*, 6638−6654.
(28) Giannozzi, P.; Baroni, S.; Bonini, N.; Calandra, M.; Car, R.; Cavazzoni, C.; Ceresoli, D.; Chiarotti, G. L.; Cococcioni, M.; Dabo, I.; Dal Corso, A.; de Gironcoli, S.; Fabris, S.; Fratesi, G.; Gebauer, R.; Gerstmann, U.; Gougoussis, C.; Kokalj, A.; Lazzeri, M.; Martin-Samos, L.; Marzari, N.; Mauri, F.; Mazzarello, R.; Paolini, S.; Pasquarello, A.; Paulatto, L.; Sbraccia, C.; Scandolo, S.; Sclauzero, G.; Seitsonen, A. P.; Smogunov, A.; Umari, P.; Wentzcovitch, R. M. QUANTUM ESPRESSO: A Modular and Open-Source Software Project for Quantum Simulations of Materials. *J. Phys.: Condens. Matter* **2009**, *21*, No. 395502.
(29) Giannozzi, P.; Andreussi, O.; Brumme, T.; Bunau, O.; Buongiorno Nardelli, M.; Calandra, M.; Car, R.; Cavazzoni, C.; Ceresoli, D.; Cococcioni, M.; Colonna, N.; Carnimeo, I.; Dal Corso, A.; de Gironcoli, S.; Delugas, P.; DiStasio, R. A.; Ferretti, A.; Floris, A.; Fratesi, G.; Fugallo, G.; Gebauer, R.; Gerstmann, U.; Giustino, F.; Gorni, T.; Jia, J.; Kawamura, M.; Ko, H.-Y.; Kokalj, A.; Küçükbenli, E.; Lazzeri, M.; Marsili, M.; Marzari, N.; Mauri, F.; Nguyen, N. L.; Nguyen, H.-V.; Otero-de-la-Roza, A.; Paulatto, L.; Poncé, S.; Rocca, D.; Sabatini, R.; Santra, B.; Schlipf, M.; Seitsonen, A. P.; Smogunov, A.; Timrov, I.; Thonhauser, T.; Umari, P.; Vast, N.; Wu, X.; Baroni, S. Advanced Capabilities for Materials Modelling with Quantum ESPRESSO. *J. Phys.: Condens. Matter* **2017**, *29*, No. 465901.
(30) Guo, Y.; Li, C.; Li, X.; Niu, Y.; Hou, S.; Wang, F. Effects of Rb Incorporation and Water Degradation on the Stability of the Cubic Formamidinium Lead Iodide Perovskite Surface: A First-Principles Study. *J. Phys. Chem. C* **2017**, *121*, 12711−12717.
(31) Moon, J.; Kwon, S.; Alahbakhshi, M.; Lee, Y.; Cho, K.; Zakhidov, A.; Kim, M. J.; Gu, Q. Surface Energy-Driven Preferential Grain Growth of Metal Halide Perovskites: Effects of Nanoimprint Lithography Beyond Direct Patterning. *ACS Appl. Mater. Interfaces* **2021**, *13*, 5368−5378.
(32) Hoell, A.; Zizak, I.; Mokrani, L. Einrichtung Zur Kleinwinkelstreumessung Zur Analyse Der Nanostruktur an Proben Mittels Röntgenstrahlung. DE102006029449B3 2007.
(33) Krumrey, M.; Ulm, G. High-Accuracy Detector Calibration at the PTB Four-Crystal Monochromator Beamline. *Nuclear Instruments & Methods in Physics Research: Section A* **2001**, *467-468*, 1175−1178.
(34) Keiderling, U. The New "BerSANS-PC" Software for Reduction and Treatment of Small Angle Neutron Scattering Data. *Appl. Phys. A: Mater. Sci. Process.* **2002**, *74*, s1455−s1457.
(35) Feigin, L. A.; Svergun, D.I. *Structure Analysis by Small-Angle X-Ray and Neutron Scattering*; Plenum Press, New York, 1987.
(36) Qin, F.; Wang, Z.; Wang, Z. L. Anomalous Growth and Coalescence Dynamics of Hybrid Perovskite Nanoparticles Observed by Liquid-Cell Transmission Electron Microscopy. *ACS Nano* **2016**, *10*, 9787−9793.
(37) Hao, X.; Chen, M.; Wang, L.; Cao, Z.; Li, Y.; Han, S.; Zhang, M.; Yu, K.; Zeng, J. *In Situ* SAXS Probing the Evolution of the Precursors and Onset of Nucleation of ZnSe Colloidal Semiconductor Quantum Dots. *Chem. Commun.* **2020**, *56*, 2031−2034.
(38) Ogle, J.; Powell, D.; Amerling, E.; Smilgies, D.-M.; Whittaker-Brooks, L. Quantifying Multiple Crystallite Orientations and Crystal Heterogeneities in Complex Thin Film Materials. *CrystEngComm* **2019**, *21*, 5707−5720.
(39) Wang, K.-H.; Li, L.-C.; Shellaiah, M.; Wen Sun, K. Structural and Photophysical Properties of Methylammonium Lead Tribromide (MAPbBr3) Single Crystals. *Sci. Rep.* **2017**, *7*, 13643.
(40) Franz, A.; Többens, D. M.; Lehmann, F.; Kärgell, M.; Schorr, S. The Influence of Deuteration on the Crystal Structure of Hybrid Halide Perovskites: A Temperature-Dependent Neutron Diffraction

https://doi.org/10.1021/acs.chemmater.3c00075
Chem. Mater. 2023, 35, 4181−4191

Study of $FAPbBr_3$. *Acta Crystallogr., Sect. B: Struct. Sci., Cryst. Eng. Mater.* **2020**, *76*, 267−274.
(41) Schueller, E. C.; Laurita, G.; Fabini, D. H.; Stoumpos, C. C.; Kanatzidis, M. G.; Seshadri, R. Crystal Structure Evolution and Notable Thermal Expansion in Hybrid Perovskites Formamidinium Tin Iodide and Formamidinium Lead Bromide. *Inorg. Chem.* **2018**, *57*, 695−701.
(42) Oner, S. M.; Sezen, E.; Yordanli, M. S.; Karakoc, E.; Deger, C.; Yavuz, I. Surface Defect Formation and Passivation in Formamidinium Lead Triiodide ($FAPbI_3$) Perovskite Solar Cell Absorbers. *J. Phys. Chem. Lett.* **2022**, *13*, 324−330.
(43) Kirstein, E.; Yakovlev, D. R.; Glazov, M. M.; Zhukov, E. A.; Kudlacik, D.; Kalitukha, I. V.; Sapega, V. F.; Dimitriev, G. S.; Semina, M. A.; Nestoklon, M. O.; Ivchenko, E. L.; Kopteva, N. E.; Dirin, D. N.; Nazarenko, O.; Kovalenko, M. V.; Baumann, A.; Höcker, J.; Dyakonov, V.; Bayer, M. The Landé Factors of Electrons and Holes in Lead Halide Perovskites: Universal Dependence on the Band Gap. *Nat. Commun.* **2022**, *13*, 3062.
(44) Tao, S.; Schmidt, I.; Brocks, G.; Jiang, J.; Tranca, I.; Meerholz, K.; Olthof, S. Absolute Energy Level Positions in Tin- and Lead-Based Halide Perovskites. *Nat. Commun.* **2019**, *10*, 2560.
(45) Butler, K. T.; Frost, J. M.; Walsh, A. Band Alignment of the Hybrid Halide Perovskites $CH_3NH_3PbCl_3$, $CH_3NH_3PbBr_3$ and $CH_3NH_3PbI_3$. *Mater. Horiz.* **2015**, *2*, 228−231.
(46) Chen, Y.; Zhou, W.; Chen, X.; Zhang, X.; Gao, H.; Ouedraogo, N. A. N.; Zheng, Z.; Han, C. B.; Zhang, Y.; Yan, H. In Situ Management of Ions Migration to Control Hysteresis Effect for Planar Heterojunction Perovskite Solar Cells. *Adv. Funct. Mater.* **2022**, *32*, 2108417.
(47) Chen, B.; Yang, M.; Priya, S.; Zhu, K. Origin of J − V Hysteresis in Perovskite Solar Cells. *J. Phys. Chem. Lett.* **2016**, *7*, 905−917.
(48) McGovern, L.; Koschany, I.; Grimaldi, G.; Muscarella, L. A.; Ehrler, B. Grain Size Influences Activation Energy and Migration Pathways in $MAPbBr_3$ Perovskite Solar Cells. *J. Phys. Chem. Lett.* **2021**, *12*, 2423−2428.
(49) Liu, P.; Wang, W.; Liu, S.; Yang, H.; Shao, Z. Fundamental Understanding of Photocurrent Hysteresis in Perovskite Solar Cells. *Adv. Energy Mater.* **2019**, *9*, 1803017.
(50) Liu, J.; Hu, M.; Dai, Z.; Que, W.; Padture, N. P.; Zhou, Y. Correlations between Electrochemical Ion Migration and Anomalous Device Behaviors in Perovskite Solar Cells. *ACS Energy Lett.* **2021**, *6*, 1003−1014.
(51) Zhu, X.; Du, M.; Feng, J.; Wang, H.; Xu, Z.; Wang, L.; Zuo, S.; Wang, C.; Wang, Z.; Zhang, C.; Ren, X.; Priya, S.; Yang, D.; Liu, S. High-Efficiency Perovskite Solar Cells with Imidazolium-Based Ionic Liquid for Surface Passivation and Charge Transport. *Angew. Chem., Int. Ed.* **2021**, *60*, 4238−4244.
(52) Oranskaia, A.; Yin, J.; Bakr, O. M.; Brédas, J.-L.; Mohammed, O. F. Halogen Migration in Hybrid Perovskites: The Organic Cation Matters. *J. Phys. Chem. Lett.* **2018**, *9*, 5474−5480.
(53) Pitarch-Tena, D.; Ngo, T. T.; Vallés-Pelarda, M.; Pauporté, T.; Mora-Seró, I. Impedance Spectroscopy Measurements in Perovskite Solar Cells: Device Stability and Noise Reduction. *ACS Energy Lett.* **2018**, *3*, 1044−1048.
(54) Yoo, S. M.; Yoon, S. J.; Anta, J. A.; Lee, H. J.; Boix, P. P.; Mora-Seró, I. An Equivalent Circuit for Perovskite Solar Cell Bridging Sensitized to Thin Film Architectures. *Joule* **2019**, *3*, 2535−2549.
(55) Zarazua, I.; Bisquert, J.; Garcia-Belmonte, G. Light-Induced Space-Charge Accumulation Zone as Photovoltaic Mechanism in Perovskite Solar Cells. *J. Phys. Chem. Lett.* **2016**, *7*, 525−528.
(56) Riquelme, A. J.; Valadez-Villalobos, K.; Boix, P. P.; Oskam, G.; Mora-Seró, I.; Anta, J. A. Understanding Equivalent Circuits in Perovskite Solar Cells. Insights from Drift-Diffusion Simulation. *Phys. Chem. Chem. Phys.* **2022**, *24*, 15657−15671.
(57) Fassl, P.; Ternes, S.; Lami, V.; Zakharko, Y.; Heimfarth, D.; Hopkinson, P. E.; Paulus, F.; Taylor, A. D.; Zaumseil, J.; Vaynzof, Y. Effect of Crystal Grain Orientation on the Rate of Ionic Transport in Perovskite Polycrystalline Thin Films. *ACS Appl. Mater. Interfaces* **2019**, *11*, 2490−2499.
(58) Eames, C.; Frost, J. M.; Barnes, P. R. F.; O'Regan, B. C.; Walsh, A.; Islam, M. S. Ionic Transport in Hybrid Lead Iodide Perovskite Solar Cells. *Nat. Commun.* **2015**, *6*, 2−9.

https://doi.org/10.1021/acs.chemmater.3c00075
Chem. Mater. 2023, 35, 4181−4191